Herschel-PACS observations of discs in the η Chamaeleontis association

Riviere-Marichalar, P.; Elliott, P.; Rebollido, I.; Bayo, A.; Ribas, A.; Merín, B.; Kamp, I.; Dent, W. R. F.; Montesinos, B.

Published in:
Astronomy and astrophysics

DOI:
10.1051/0004-6361/201526584

Publication date:
2015

A&A 584, A22 (2015)
DOI: 10.1051/0004-6361/201526584

Astronomy & Astrophysics

Herschel-PACS observations of discs in the η Chamaeleontis association⋆

P. Riviere-Marichalar[1], P. Elliott[2,3], I. Rebollido[1], A. Bayo[4,5], A. Ribas[1], B. Merín[1], I. Kamp[6], W. R. F. Dent[7], and B. Montesinos[8]

[1] European Space Astronomy Centre (ESA), PO Box 78, 28691 Villanueva de la Cañada, Madrid, Spain
e-mail: priviere@sciops.esa.int
[2] European Southern Observatory, Alonso de Cordova 3107, Vitacura Casilla 19001, Santiago 19, Chile
[3] School of Physics, University of Exeter, Stocker Road, Exeter, EX4 4QL, UK
[4] Instituto de Física y Astronomía, Facultad de Ciencias, Universidad de Valparaíso, Av. Gran Bretaña 1111, 5030 Casilla, Valparaíso, Chile
[5] ICM nucleus on protoplanetary discs, Universidad de Valparaíso, Av. Gran Bretaña 1111, Valparaíso, Chile
[6] Kapteyn Astronomical Institute, University of Groningen, PO Box 800, 9700 AV Groningen, The Netherlands
[7] ALMA, Avda Apoquindo 3846, Piso 19, Edificio Alsacia, Las Condes, Santiago, Chile
[8] Depto. Astrofísica, Centro de Astrobiología (CAB, INTA–CSIC), PO Box 78, ESAC Campus, 28691 Villanueva de la Cañada, Madrid, Spain

Received 22 May 2015 / Accepted 2 October 2015

ABSTRACT

Context. Protoplanetary discs are the birthplace of planets. Studying protoplanetary discs is the key to constraining theories of planet formation. By observing dust and gas in associations at different ages we can study the evolution of these discs, their clearing timescales, and their physical and geometrical properties.The stellar association η Cha is peculiar; some members still retain detectable amounts of gas in their discs at the late age of ∼7 Myr, making it one of the most interesting young stellar associations in the solar neighbourhood.

Aims. We characterise the properties of dust and gas in protoplanetary and transitional discs in the η Cha young cluster, with special emphasis on explaining the peculiarities that lead to the observed high disc detection fraction and prominent IR excesses at an age of ∼7 Myr.

Methods. We observed 17 members of the η Cha association with *Herschel*-PACS in photometric mode and line spectroscopic mode. A subset of members were also observed in range spectroscopic mode. The observations trace [OI] and H_2O emissions at 63.18 and 63.32 μm, respectively, as well as CO, OH, CH^+, and [CII] at different wavelengths for those systems observed in range mode. The photometric observations were used to build complete spectral energy distributions (SEDs) from the optical to the far-IR. High-resolution multi-epoch optical spectra with high signal-to-noise ratios were also analysed to study the multiplicity of the sources and look for further gas (accreting) and outflow indicators.

Results. We detect four out of fifteen sources observed at 70 μm, four out of six at 100 μm, and six out of sixteen at 160 μm. Only one system shows [OI] emission at 63 μm, namely RECX 15 or J0843.3-7905. None of them shows far-IR line emission at any other wavelength. The [OI] emission toward RECX 15 points to the presence of an outflow; however, the emission is not extended. We study H_α emission among η Cha members and conclude that RECX 4, 5, 9, 11, and 15 are actively accreting in at least one epoch.

Conclusions. The SEDs of the discs in η Cha show a variety of shapes, from those in Taurus and in Upper Scorpius to sources showing excess over the Taurus median SED. Furthermore, the SEDs of RECX 3 and RECX 4 are typical of debris discs. The detection fraction for [OI] in η Cha is lower than younger regions like Taurus and Cha II, indicative of an evolutionary trend. The lack of [OI] emission, together with the intermediate values of the IR excess, can be explained by long-lived discs with a flattened geometry or by flared discs with a low UV flux, or by a combination of the two scenarios.

Key words. circumstellar matter – binaries: spectroscopic – stars: formation – astrochemistry

1. Introduction

Planets are born in protoplanetary discs that surround young stars. The study of both gas and dust evolution in protoplanetary discs is therefore a major step to constraining planet formation theories. In the last three decades we have acquired extensive knowledge on the evolution of the dust phase (see Williams & Cieza 2011). One of the most prominent discoveries related to dust evolution is that protoplanetary discs develop inner disc opacity holes, leading to the formation of the so-called transitional discs (Strom et al. 1989). These transitional discs seem to be a transient stage before the fast dissipation (<0.5 Myr, Skrutskie et al. 1990) of the protoplanetary disc on timescales of <10 Myr (see Williams & Cieza 2011, for a review).

Because there are both observational and computational difficulties, we still lack a good description of the evolution of the gas phase, even if gas dominates the mass budget of protoplanetary discs. The most abundant gas species, H_2, lacks a permanent electric dipole, making IR rotational transitions weak. After H_2, CO is the most abundant molecule and it has been traditionally used to study the gas mass. However, CO lines are usually

⋆ *Herschel* is an ESA space observatory with science instruments provided by European-led Principal Investigator consortia and with important participation from NASA.

Table 1. Stellar parameters for η Cha members observed with *Herschel*-PACS.

Source	Sp. type	$T_{\rm eff}$	L_*
–	–	(K)	$L_\odot$
RECX 1	K4	4100	0.96 ± 0.52
RECX 3	M3	3200	0.09 ± 0.05
RECX 4	K7	3600	0.23 ± 0.13
RECX 5	M5	3000	0.06 ± 0.03
RECX 6	M2	3300	0.11 ± 0.06
RECX 7	K3	4100	0.70 ± 0.38
RECX 8	A7	6600	23 ± 2
RECX 9	M4	3300	0.09 ± 0.05
RECX 10	M0	3800	0.22 ± 0.12
RECX 11	K5	4100	0.55 ± 0.30
RECX 12	M3	3300	0.24 ± 0.13
RECX 13 (HD 75505)	A1	8000	7.2 ± 4.0
RECX 14 (J0841.5-7853)	M4	2900	0.02 ± 0.01
RECX 15 (J0843.3-7905)	M2	3300	0.08 ± 0.04
RECX 16 (J0844.2-7833)	M5.5	2900	0.02 ± 0.01
RECX 17 (J0838.9-7916)	M5	3100	0.04 ± 0.02
RECX 18 (J0836.2-7908)	M5.5	2900	0.02 ± 0.01

Notes. Spectral types from Zuckerman & Song (2004).

optically thick. Furthermore, CO can be frozen in the mid-plane of the disc, and photodissociated in the disc atmosphere (Aikawa et al. 1996; Gorti & Hollenbach 2008), making it a poor tracer of the total disc gas mass in some cases. The gas-to-dust ratio has a dramatic influence in shaping the disc and in the subsequent planet formation (Pinte & Laibe 2014). Therefore, determining the gas-to-dust ratio in different disc conditions is crucial to understanding planet formation. Typically, a gas-to-dust ratio of 100 has been assumed, based on the ISM value. However, recent studies show that the actual ratio might be smaller (see e.g. Thi et al. 2010). Williams & Best (2014) show that the combination of ^{13}CO and C^{18}O provides a good estimate of the gas mass. To further constrain the geometry of the disc, we need observations of other atomic and molecular species, typically in the near- to far-IR, such as O and H_2O.

An additional caveat in studying the evolution of gas in protoplanetary discs is that the age of individual systems is hard to constrain (Soderblom et al. 2014). Therefore, we must use stars belonging to young clusters and stellar associations because the mean age of their members is well known. We can compare the disc frequency and properties of discs in stellar associations at different ages to perform evolutionary studies.

The η Cha cluster is a young stellar association with an age of 5–9 Myr (Mamajek et al. 1999; Lawson et al. 2001; Luhman & Steeghs 2004a), located at a distance of 97 pc to the Sun. Luhman & Steeghs (2004a) propose a list of 18 cluster members within a radius of 0.5 pc from the cluster centre with spectral types in the range B8-M5.5, where most members (15) belong to types K and M.

The cluster shows a deficit of low-mass stars ($M < 25\ M_{\rm Jup}$ Lyo et al. 2006). However, it is not clear whether the census of members is complete. By comparing the IMF of η Cha with that of the Trapezium cluster, Lyo et al. (2004) predict 20-29 undiscovered low-mass stars and brown dwarfs ($0.025 < M_*/M_\odot < 0.15$), meaning that the number of undetected members could be similar to the number of actual members. Different surveys (Luhman & Steeghs 2004a; Song et al. 2004; Lyo et al. 2006) looked for new cluster members up to 2.6 pc from the centre with no success. More recently, Murphy et al. (2010) proposed three new candidate members at distances between 2.6 and 10 pc from the cluster centre in the mass range $0.08 < M_*/M_\odot < 0.3$. The presence of mass segregation was shown by Lyo et al. (2004), who claimed that 50% of the cluster mass is located inside the inner 0.17 pc. Low-mass members could be located at greater distances (making them harder to detect) in a low-mass cluster halo, either due to dynamical interactions or to mass segregation during cluster relaxation.

Gautier et al. (2008) computed a disc fraction of 56% at 24 μm, and a lower limit of 31% at 70 μm, considered high for a ~7 Myr old cluster. This high disc detection fraction was later confirmed by Sicilia-Aguilar et al. (2009) making use of *Spitzer*-IRS spectroscopic observations of the cluster. However, when discussing the detection fraction one has to remember that the census of η Cha members might be incomplete (see previous paragraph). If the low-mass members escaping detection are mostly disc-less stars the disc fraction could dramatically fall. Fang et al. (2013) showed that evolution in loose environments, such as in η Cha, proceeds more slowly than in more crowded associations, a fact that may explain the high number of disc detections in η Cha. Furthermore, the presence of a disc seems to be linked to single stars, as only one η Cha disc is detected surrounding a binary system (Bouwman et al. 2006). The authors showed that the system is a wide binary, and the disc is most likely circumprimary, and concluded that binarity results in shorter disc clearing timescales.

In this paper we present photometric and spectroscopic *Herschel*-PACS observations of the η Cha cluster, as well as VLT/UVES spectroscopic observations. We discuss the implications of our observations for the peculiarities of the η Cha cluster discussed in the previous paragraph. In Sect. 2 we describe the sample properties and observations performed, and the data reduction process. In Sect. 4 we present the main results from our photometric and spectroscopic survey. In Sect. 5 we discuss the main implications of our results and in Sect. 6 we present an overview of the contents of this study.

2. Sample and observations

The GAs Survey of Protoplanetary Systems program (GASPS; Dent et al. 2013) observed more than 250 stars in seven young stellar associations with ages in the range 1–30 Myr, including 17 young stellar objects belonging to the η Cha stellar association. We included all the η Cha members with spectral types in the range A1-M5.5. We compiled archival and literature photometry for each η Cha member in the sample, including 2MASS (Skrutskie et al. 2006), WISE (Wright et al. 2010), AKARI-IRC (Ishihara et al. 2010), optical photometry (Bessel 1990; Lawson et al. 2001; Lyo et al. 2004), and *Spitzer* photometry (Gautier et al. 2008; Megeath et al. 2005).

We obtained PACS photometric observations of 17 sources: 16 objects were observed at 70 μm, 7 were also observed at 100 μm, and one source was observed only at 100 μm (the PACS observational IDs for each source are given in Table 2). Since PACS simultaneously observes at either 70 or 100 μm, and at 160 μm, we always have observations at 160 μm. The photometric observations were made in ScanMap mode. For most objects, at least two images were obtained in the blue channel (70 or 100 μm) with complementary angles (70° and 110°) to increase the signal-to-noise ratio (S/N) once combined. Total integration times, after co-adding, range from 133 s to 2464 s at 70 μm, 552 s to 1122 s at 100 μm, and 552 s to 2464 s at 160 μm. The GASPS photometry, together with archival and literature photometry, was used to compile spectral energy

Table 2. Observation log.

Source (RECX)	Phot Obs. ID (1342000000+)	Spec Obs. ID (1342000000+)
1	209480, 209481	210391
3	88884, 11967, 211968-211970	210389
4	211963-211966	199241
5	195468, 211977, 211978	210392
6	211981, 211982	223114
7	189366, 211961, 211962, 187338	–
8	189366, 211961, 211962, 187338	223113
9	211975, 211976	223112
10	221134, 221135	223111
11	189387, 211973, 211974	223115
12	211979, 211980	223110
13	189367, 211971, 211972	–
14	189368, 1342221278, 1342221278	210390
15	189366, 211961, 211962, 187338	210388
16	221276, 221277	210387
17	195469, 209484, 209485	–
18	189365, 209482, 209483	–

Notes. Values separated by - indicate ranges of Obs. IDs.

distributions (SEDs) for η Cha members from optical to far-IR wavelengths.

We spectroscopically observed all the η Cha members known to show IR excess (seven sources) plus a subsample of six members without a known IR excess, for a total of thirteen members observed. Spectroscopic observations aimed to detect emission from the [OI] $^3P_1 \rightarrow {}^3P_2$ transition at 63.185 μm (spectroscopic observational IDs are given in Table 2). We also obtained PACS range spectroscopic observations of the three sources with largest disc fractional luminosity, namely RECX 5, RECX 11, and RECX 15, to detect CO, OH, H_2O, and [CII] emission. They were observed at 72 and 78 μm in the blue bands and at 145 and 158 μm in the red bands. RECX 15 was also observed at 89 and 190 μm.

Aiming to better characterise gas emission in η Cha and to look for close, spectroscopic binaries (SB), we queried the ESO archive for high-resolution optical spectroscopic observations and found publicly available data obtained with VLT/UVES. Ten out of seventeen objects had been observed previously. We have three epochs of observations for most sources, with the exception of RECX 1, which only has two epochs, and RECX 3 and 5, which have four epochs. The time coverage was not homogeneous, covering timelines from one day to one month.

We used the Virtual Observatory SED Analyzer (VOSA Bayo et al. 2008, 2014) to enlarge the wavelength range of the SED of our targets. VOSA queries a number of VO-compliant services to look for photometry as well as other relevant parameters such as distances, extinction measurements in the line of sight. Our most complete SEDs cover from Strömgren photometry to far infrared *Spitzer*/MIPS bands. VOSA offers the possibility to automatically look for infrared excess in the compiled SEDs. The original methodology was to estimate sequentially the infrared slope α, with a starting point at 2 μm, adding redder photometric points one at a time. The comparison of this iterative calculated α with the classical Lada & Lada (Lada 1987) parametrisation allowed us to detect the start of the departure from the purely photospheric behaviour. In the newest version of VOSA (Bayo et al. 2014), the method for detecting outliers (data-points with reliable quality flags, but for some reason a flux value that seem to deviate from the remaining SED) has been refined, the excess in two consecutive bands must be detected before flagging those as non-purely photospheric, and the estimation of the deviation from purely photospheric flux is also provided.

We also took advantage of the two statistical approaches VOSA offers for determining stellar parameters. On the one hand it runs through the grids of models available in the VO and provides the one that minimises the residuals (to be used to build an object-by-object-based panchromatic bolometric correction), and on the other hand it proceeds in a Bayesian framework providing the individual probability density functions (PDFs) for each parameter and object. Both approaches agree within the uncertainties/limitations characterising each one, the grid step and the standard deviation of the PDFs, respectively. Complete SEDs were used to compute the stellar parameters, assuming $A_V = 0$ (see extinctions for RECX 11 and RECX 15 in McJunkin et al. 2014). The derived parameters are shown in Table 1. Spectral types are taken from Zuckerman & Song (2004). Our stellar parameters for K and M stars agree well with those in Luhman & Steeghs (2004a), with a mean difference in $T_{\rm eff}$ of 120 K. However, early-type stars show a more pronounced difference: 1000 K for RECX 8, and 1230 K for RECX 13. The difference might be due to incorrect spectral classification or to a poor coverage of the SED peak emission, which is of main importance to fitting models to SEDs. However, the effective temperature of the sources does not affect the results from this paper, and a proper discussion of the differences is beyond its scope.

3. Data reduction

3.1. PACS photometric data reduction

The reduction of PACS photometric data was carried out using HIPE 12.0[1] (calibration tree version 65) and the high-pass filtering pipeline for small scan maps. The reduction process includes the following main steps: bad and saturated pixel flagging, flat field correction, deglitching, and high-pass filtering. When several images were available for the same source at the same wavelength, they were combined to increase the S/N. The photometric maps were projected onto the final images with a pixel scale of 2 arcsec/pixel for the 70 and 100 μm bands and of 3 arcsec/pixel for the 160 μm band. The maps were also projected onto images with the native pixel size (3.2, 3.2, and 6.4 arcsec/pixel for the 70, 100, and 160 μm bands, respectively) to minimise the impact of correlated noise in photometric uncertainties. The final maps are shown in Figs. 1–3 with a pixel scale of 1″/pixel.

Aperture photometry was computed using apertures of 6, 6, and 12″ for the 70, 100, and 160 μm bands, respectively. The sky annulus was placed at 25″ from the source with a width to 10″. To retrieve the final fluxes we applied aperture corrections from the proper calibration files (version 65).

Photometric errors consist of the quadratic sum of the noise errors and the calibration errors. Noise errors were computed as the standard deviation of the sky scaled to the size of the aperture radius. The resulting uncertainties were scaled according to the correlated noise correction factor (*cnc*),

$$cnc = a \times (pxs/pxs_0)^b, \quad (1)$$

where pxs is the pixel size of the processed image, pxs_0 is the native pixel size (3.2 for the 70 and 100 μm bands and 6.4 for

[1] http://herschel.esac.esa.int/hcss-doc-12.0/

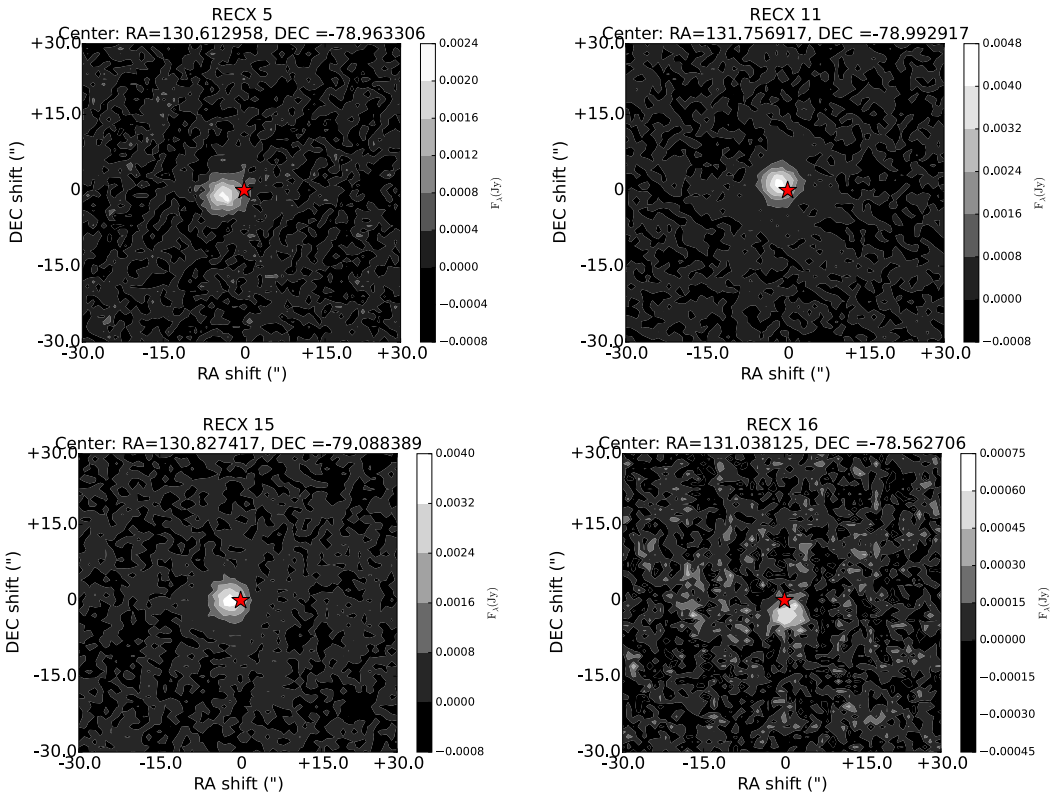

Fig. 1. Contour plots for PACS images at 70 μm. The red star gives the nominal position of the star.

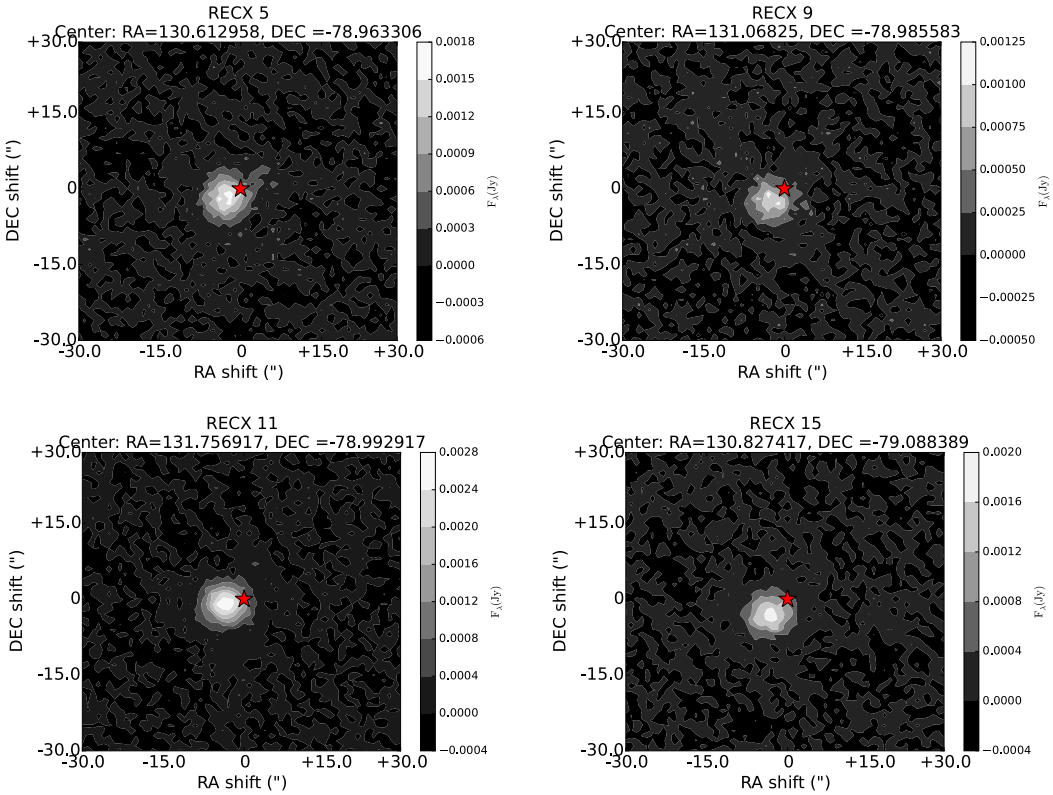

Fig. 2. Contour plots for PACS images at 100 μm. The red star gives the nominal position of the star.

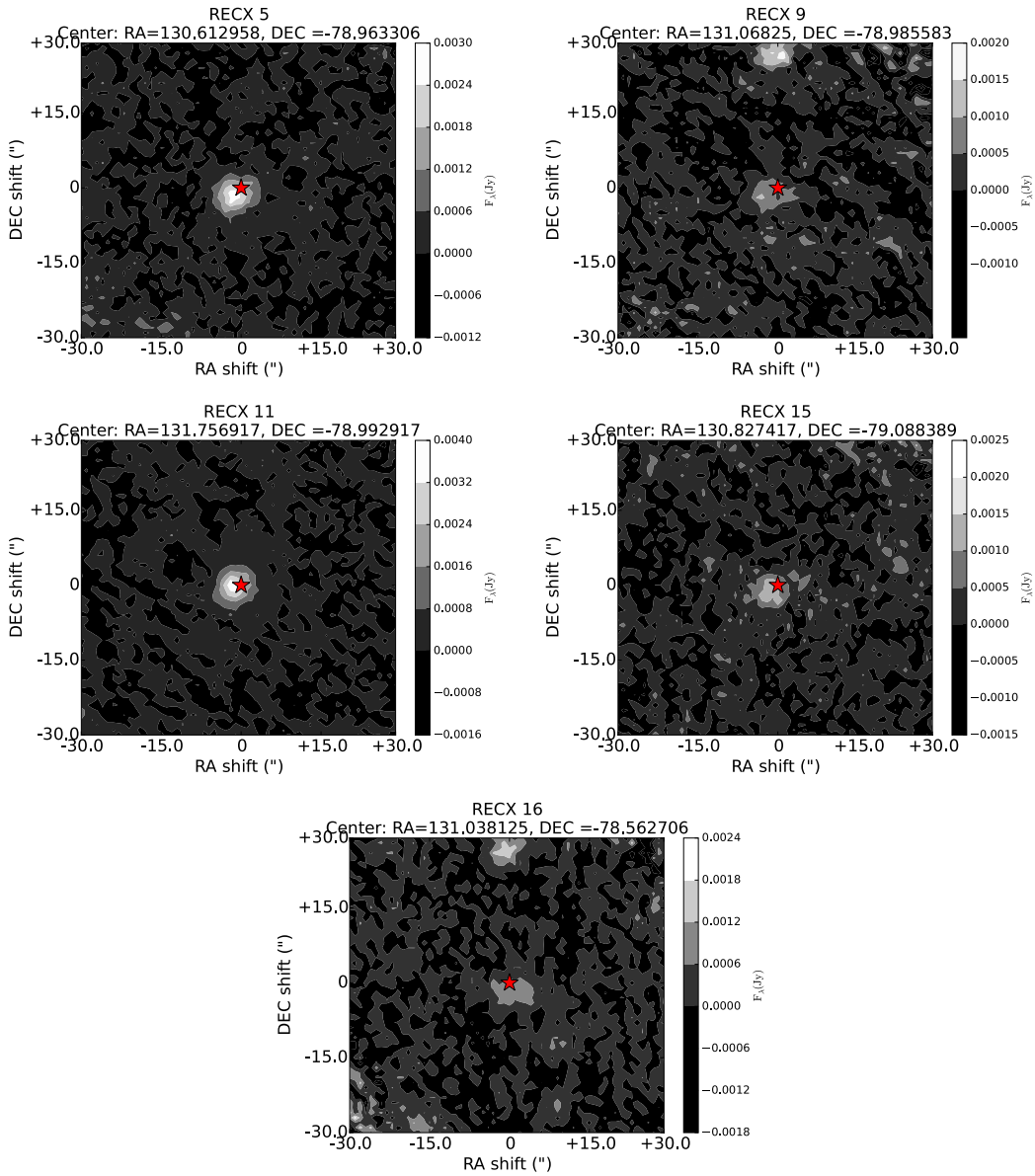

Fig. 3. Contour plots for PACS images at 160 μm. The red star gives the nominal position of the star.

the 160 μm band), and a and b are numerical factors that depend on the band selected, being $a = 0.95$, $b = 1.68$ for the 70 and 100 μm bands, and $a = 0.88$, $b = 1.73$ for the 160 μm band (Balog et al. 2014). Calibration errors are 2.64%, 2.75%, and 4.15% for the 70, 100, and 160 μm bands, respectively[2]. In a similar way, upper limits on flux densities for non-detected sources were computed as the standard deviation of the sky annulus centred at the nominal position of the star. Upper limits were then scaled to the number of pixels inside the aperture and aperture corrected. Photometric fluxes and uncertainties, together with 3σ upper limits for non-detected sources are shown in Table 3.

3.2. PACS spectroscopic data reduction

The reduction of PACS spectroscopic data was performed using HIPE 12.0 following the standard procedure for PACS spectroscopic data reduction. A major step when extracting line fluxes from the PACS IFU is to detect where the source is centred. To that aim, the flux in the continuum in each spaxel must be evaluated and the flux distribution compared to a theoretical one from model PSFs. For η Cha members, the final spectra were extracted from the central spaxel as all the observations were properly centred on the source of interest and aperture corrected to account for flux losses. Owing to the high noise in the edge of the spectra, we only analyse data in the range $63.0 < \lambda/\mu\text{m} < 63.4$ for line observations. The limits for range observations were $72.0 < \lambda/\mu\text{m} < 73.0$, $78.5 < \lambda/\mu\text{m} < 79.5$, $89.5 < \lambda/\mu\text{m} < 90.5$, $144.0 < \lambda/\mu\text{m} < 146.0$, $157.0 < \lambda/\mu\text{m} < 159.0$, and $179.0 < \lambda/\mu\text{m} < 181.0$.

Since the spectral ranges are short, we used first-order polynomials to fit the continuum in regions where no line emission is expected and performed Gaussian fits to continuum subtracted spectra. The line fluxes were computed as the integral of a Gaussian with the parameters coming from the fit. The uncertainties in line fluxes were computed as the integral of a Gaussian with a peak equal to the noise level, and width equal to that of the fit. When no line emission is detected ($S/N < 3$), we compute

[2] http://herschel.esac.esa.int/twiki/bin/view/Public/PacsCalibrationWeb

Table 3. *Herschel*-PACS photometry for η Cha members. Upper limits are 3σ.

Source	$F_{70\ \mu m}$	$F_{100\ \mu m}$	$F_{160\ \mu m}$	L_{IR}/L_*
(RECX)	(mJy)	(mJy)	(mJy)	–
1	<6	–	<16	$<1.8\times10^{-4}$ ($<1.9\times10^{-4}$)
3*	<7 (6 ± 1)	<10	<13	7.4×10^{-4} (7.4×10^{-4})
4*	<9 (9 ± 1)	<9	<14	7.5×10^{-4} (7.5×10^{-4})
5	113 ± 24	203 ± 13	138 ± 28	0.103 (0.082)
6	<5	–	<13	$<9.7\times10^{-4}$ ($<4.5\times10^{-4}$)
7	<15	<11	<21	$<4.3\times10^{-4}$ ($<3.0\times10^{-4}$)
8	<15	<11	<21	$<2.8\times10^{-5}$ ($<1.2\times10^{-5}$)
9	–	77 ± 3	53 ± 7	0.0158
10	<7	–	<14	$<7.3\times10^{-4}$ ($<3.4\times10^{-4}$)
11	212 ± 21	205 ± 13	174 ± 26	0.222 (0.269)
12	<5	–	<13	$<3.3\times10^{-4}$ ($<1.5\times10^{-4}$)
13	<7	–	<19	$<2.6\times10^{-5}$ ($<1.5\times10^{-5}$)
14	<15	<12	<25	0.035 (0.037)
15	204 ± 6	142 ± 5	71 ± 7	0.399 (0.578)
16	29 ± 4	–	59 ± 8	0.068 (0.085)
17	<8	–	<15	$<3.1\times10^{-3}$ ($<2.3\times10^{-3}$)
18	<10	–	<24	$<6.3\times10^{-3}$ ($<3.2\times10^{-3}$)

Notes. (*) we show 70 μm PACS fluxes by Cieza et al. (2013) in brackets. For the IR excess, we show in brackets the value computed using photometry with $\lambda \leq 70\ \mu$m.

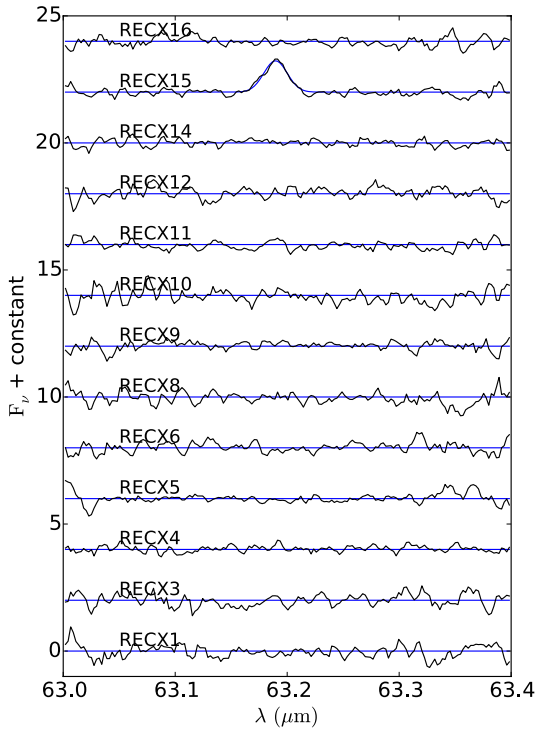

Fig. 4. Continuum subtracted PACS spectra at 63 μm. The blue line shows a fit to the continuum plus line emission.

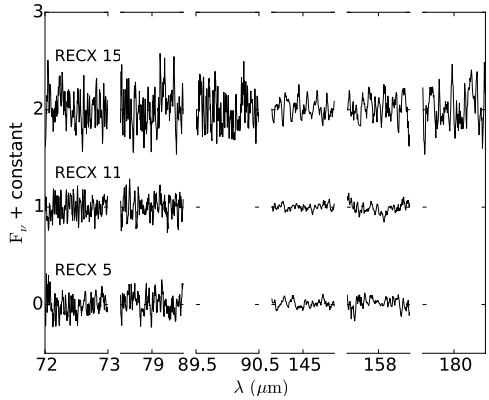

Fig. 5. From top to bottom: continuum subtracted PACS range spectra for RECX 15, RECX 11, and RECX 5.

upper limits in the same way as we compute errors, but with a FWHM equal to the instrumental value. The spectra for η Cha sources observed with PACS at 63 μm are shown in Fig. 4. The spectra for sources observed in the range 72–180 μm are shown in Fig. 5. Line fluxes and 3σ upper limits for line and range spectroscopy are shown in Tables 4 and 5, respectively.

Table 4. Line fluxes and 3σ upper limits of [OI] and o-H_2O at 63 μm.

Source	$F_{[OI]}$ (63.18 μm)	$F_{o\text{-}H_2O}$ (63.32 μm)
	(10^{-18} W/m^2)	(10^{-18} W/m^2)
RECX 1	<11	<11
RECX 3	<10	<10
RECX 4	<5.0	<5.0
RECX 5	<9.2	<9.2
RECX 6	<9.0	<9.0
RECX 8	<9.8	<9.8
RECX 9	<7.6	<7.6
RECX 10	<13	<13
RECX 11	<6.6	<6.6
RECX 12	<11	<11
RECX 14	<6.4	<6.4
RECX 15	24.0 ± 2.5	<5.6
RECX 16	<7.3	<7.3

3.3. UVES spectroscopic data reduction

UVES performs at a resolution of 40 000 with a 1″ slit. Observations of ten η Cha members were retrieved from the archive. These observations were conducted using the standard set-up, a 1″ slit width which covers the wavelength range 3250–6800 Å. All data were reduced using the

Table 5. 3σ upper limits from range spectroscopic observations in the 72–180 μm range.

Species	Line flux (W/m^2)		
	RECX 5	RECX 11	RECX 15
o – H_2O			
71.94 μm	<3.9	<4.0	<6.8
78.74 μm	<6.1	<7.6	<10.0
179.53 μm	–	–	<6.7
180.49 μm	–	–	<6.7
p – H_2O			
89.99 μm	–	–	<9.5
144.52 μm	<2.5	<1.6	<4.4
158.31 μm	<3.3	<3.6	<6.9
CO			
72.84 μm	<3.9	<4.0	<6.8
79.36 μm	<6.1	<7.6	<10.0
90.16 μm	–	–	<9.5
144.78 μm	<2.5	<1.6	<4.4
OH			
79.11 μm	<6.1	<7.6	<10.0
79.16 μm	<6.1	<7.6	<10.0
CH^+			
72.14 μm	<3.9	<4.0	<6.8
90.02 μm	–	–	<9.5
179.61 μm	–	–	<6.7
[OI] 145.52 μm	<2.5	<1.6	<4.4
[CII] 157.74 μm	<3.3	<3.6	<6.9

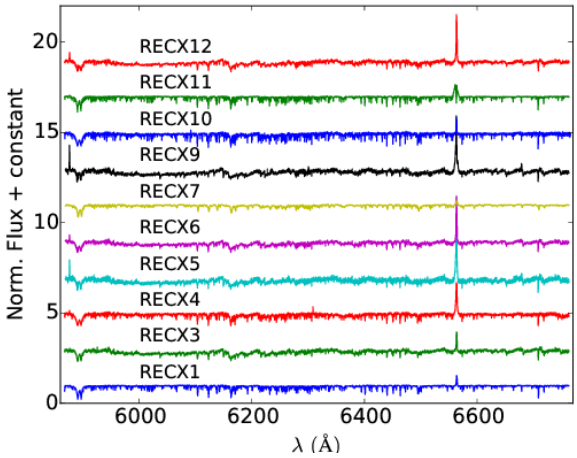

Fig. 6. UVES spectra of η Cha members.

UVES pipeline recipe uves_obs_redchain with the command-line driven utility esorex (bias corrected, dark current corrected, flat-fielded, wavelength-calibrated, and extracted). In Fig. 6 we show the average spectrum from all epochs for each η Cha member observed with UVES.

Radial velocity (RV) values were computed by means of computed cross-correlation functions (CCFs) for all reduced spectra. To compute the CCF, the observed spectrum is convolved with a CORAVEL-type numerical mask, as described in Queloz et al. (1995), K-type or M-type, depending on the spectral type of the star. The shape of the CCF function is approximated by a Gaussian profile. The RV is the peak of this profile to which the barycentric correction is applied. The average measured values can be seen in Table 6.

Table 6. Radial velocities from UVES high-resolution spectra.

Source	$\langle V_r \rangle$ (km s^{-1})	σ_{V_r} (km s^{-1})	Epochs
RECX 1	18.3	1.0	2
RECX 3	17.5	0.5	4
RECX 4	17.8	0.5	3
RECX 5	17.2	0.6	4
RECX 6	18.1	1.5	3
RECX 7	43.9	22.6	3
RECX 9	18.5	0.7	3
RECX 10	17.5	0.2	3
RECX 11	17.5	0.8	3
RECX 12	23.3	0.9	3

4. Results

4.1. Herschel-PACS photometry

We detected four out of sixteen sources observed at 70 μm, leading to a detection fraction of $0.25^{+0.13}_{-0.08}$ (with errors coming from binomial population distributions, see e.g. Burgasser et al. 2003). Two sources in the sample, namely RECX 3 and RECX 4, were not detected at 70 μm in our survey, but Cieza et al. (2013) detected both at 70 μm. Fluxes are shown in brackets in Table 3. Including these 70 μm detections, the detection fraction grows to $0.47^{+0.12}_{-0.11}$, compatible with the fraction computed by Sicilia-Aguilar et al. (2009) using *Spitzer* data. Since RECX 3 and RECX 4 resemble debris discs (see Sect. 5.1), the primordial disc fraction at 70 μm remains 0.25. Only eight objects were observed at 100 μm, and we detected four of them (0.50 ± 0.16 detection fraction). Finally, we detected five objects at 160 μm out of seventeen observed, leading to a detection fraction of $0.29^{+0.13}_{-0.08}$.

All the detected fluxes are in excess above the photosphere and we observe no correlation of the excess with $T_{\rm eff}$ or spectral type, as already observed for TW Hydra Associations (TWA) and Beta Pictoris Moving Group (BPMG) stars (Riviere-Marichalar et al. 2013, 2014). For RECX 16 this is the first detection of the source in the far-IR, both at 70 and 160 μm. For RECX 9 and RECX 15, PACS fluxes are the first detections at 100 and 160 μm, but 70 μm emission was previously detected with *Spitzer* (Gautier et al. 2008). For these three sources, PACS detections add important data to the SED and allow for a more accurate characterisation. Fluxes at 70 μm for three objects observed with PACS and MIPS (Gautier et al. 2008) agree well within the errors, except for RECX 11 where the PACS flux is larger even when errors are included which leads to a difference of 20%. Interestingly, the change at 160 μm goes in the other direction, with the MIPS flux being 20% larger than the PACS flux. Confirming whether this is real variability requires more observations. If the variability is real it may reflect a fast change in disc properties.

To test whether the emission was extended at any wavelength, we performed azimuthally averaged radial profiles of the sources, and compared the resulting profiles with that of the standard star α Boo. None of the sources showed extended emission at any wavelength.

4.2. Herschel-PACS spectroscopy

We have detected [OI] emission at 63.18 μm towards only one of the sources observed, leading to a total detection fraction of $0.08^{+0.14}_{-0.03}$. The detection fraction is low when compared to

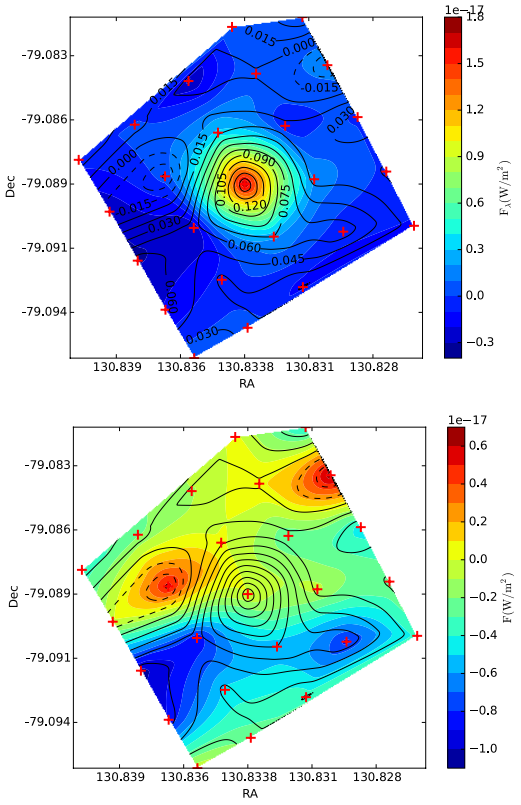

Fig. 7. *Top*: contours for line (coloured contours) and continuum at 63 μm emission in RECX 15 (solid and dashed line contours, where dashed lines represent negative values). Continuum units are in Jy. *Bottom*: line residual emission for RECX 15 at 63 μm (see Sect. 4.2) from the tests by Podio et al. (2012). Continuum contours are also shown, following the *top panel*. Red plus signs mark the central positions of the PACS spectrometer spaxels. No significant residual emission is detected.

younger associations like Taurus (0.57 ± 0.09, Howard et al. 2013) and Cha II ($0.37^{+0.12}_{-0.09}$, Riviere-Marichalar et al. 2015). This decrease with age is indicative of an evolutionary trend. The fraction of sources with an IR excess that show an [OI] detection is $0.17^{+0.23}_{-0.06}$. No H_2O emission was detected in the sample. The only source with an [OI] detection at 63.185 μm is RECX 15, which was discussed in detail in Woitke et al. (2011). [OI] emission at 63 μm is observed only in the central spaxel. In the top panel of Fig. 7 we show the spatial distribution of [OI] emission at 63.185 μm (colored contours), where we can see that the [OI] emission coincides with the continuum emission (line contours) at 63 μm. To further test whether the emission was extended, we performed a test based on the method by Podio et al. (2012), which makes use of the ratio of the line to continuum emission in each spaxel compared to that where the source is centred. The result of this test is shown in the bottom panel of Fig. 7. No significant residual emission is detected outside the central spaxel; therefore the [OI] line emission is centred at the position of the source (to the limit of PACS spatial resolution) and is not extended compared to the model PSF.

No species were detected at longer wavelengths for any of the sources (see Fig. 5). Upper limits on line fluxes for wavelengths in the range 72 to 180 μm are provided in Table 5. Dent et al. (2013) showed that the detection fraction in the GASPS sample was ~50% compared to ~10% for the other lines. Therefore, the lack of detections for the other transitions fits well with our expectations.

5. Discussion

5.1. Spectral energy distributions and infrared excesses

We complemented PACS observations with photometry at different wavelengths from public catalogues and the literature, including optical, near- and far-IR photometry (see Sect. 2). We also obtained *Spitzer*-IRS data from the Cornell Atlas of *Spitzer*-IRS Sources (CASSIS Lebouteiller et al. 2011) and included them in the SED. The resulting SEDs are shown in Fig. 8.

Gautier et al. (2008) used *Spitzer* observations to compute fractional disc luminosities for η Cha members up to 70 μm. We extended the exercise up to 160 μm by including *Herschel*-PACS observations presented in this paper. We computed the fractional disc luminosity by fitting a third-degree spline to the observed data and the photospheric model. The photospheric contribution spline is then subtracted from the observed data spline to get the excess luminosity. For objects that were not detected with PACS we used the lowest upper limits available as detections to derive upper limits on the IR excess. The IR excesses are shown in Table 3. Since some sources were only detected at 70 μm (namely RECX 3 and RECX 4) we also computed the fractional disc luminosities using only photometry ≤70 μm. Luminosities computed in this way are shown in brackets in Table 3.

In Fig. 9 we show histograms of the fractional disc luminosities ($L_{\rm IR}/L_*$, computed using the whole spectral range available) for detected sources and of upper limits for non-detected sources, with bin sizes computed using the Freedman-Diaconis rule (Freedman & Diaconis 1981). For RECX 3 and RECX 4 the fluxes from Cieza et al. (2013) were used. There is small overlap between both distributions due to the very small fractional disc luminosities shown by RECX 3 and RECX 4 ($L_{\rm IR}/L_* \sim 7 \times 10^{-4}$); $L_{\rm IR}/L_* < 10^{-3}$ for most non-detected sources, with only two non-detected sources with excesses in the range 10^{-3}–10^{-2}, namely RECX 17 and RECX 18.

Among the five objects detected at 160 μm with PACS, only RECX 5 and RECX11 were previously detected at 160 μm with *Spitzer*-MIPS by Gautier et al. (2008). Our infrared excess for RECX 5 is 0.085, in good agreement with Gautier et al. (2008). For RECX 11, however, our fractional disc luminosity is more than four times larger. RECX 9, 15, and 16 were not detected at 160 μm by *Spitzer*-MIPS, so our detections at 160 μm are crucial for deriving more accurate fractional disc luminosities. For RECX 9 the fractional disc luminosity remains unchanged, while for RECX 15 and 16 our excesses are 2.0 and 1.7 times larger, respectively. RECX 3 and RECX 4 show fractional disc luminosities typical of optically thin debris discs. Our fractional disc luminosities for these sources are larger than the values computed by Gautier et al. (2008) using MIPS at 24 μm.

Gautier et al. (2008) showed that the fractional disc luminosity in RECX 15 is typical of T Tauri stars. RECX 5, 9, 14, and 16 show fractional disc luminosities in the range 0.03 to 0.1. Gautier et al. (2008) points out that these excesses are between those of optically thick discs surrounding young stars (like in RECX 15 and 11) and debris discs, and propose that a likely explanation for these intermediate excesses is an optically thick disc that has experienced flattening. We see in Sect. 5.2.2 how flat discs can explain the lack of [OI] detections for those sources. The low-IR excesses ($L_{\rm IR}/L_* < 10^{-3}$) shown by RECX 3 and RECX 4 are typical of optically thin debris discs.

In Fig. 10 we compare the SEDs of η Cha stars with a detected excess in the far- or mid-IR with the median SED of Taurus and Upper Scorpius from Mathews et al. (2013). Both RECX 3 and RECS 4 SEDs fall well below the median SED for

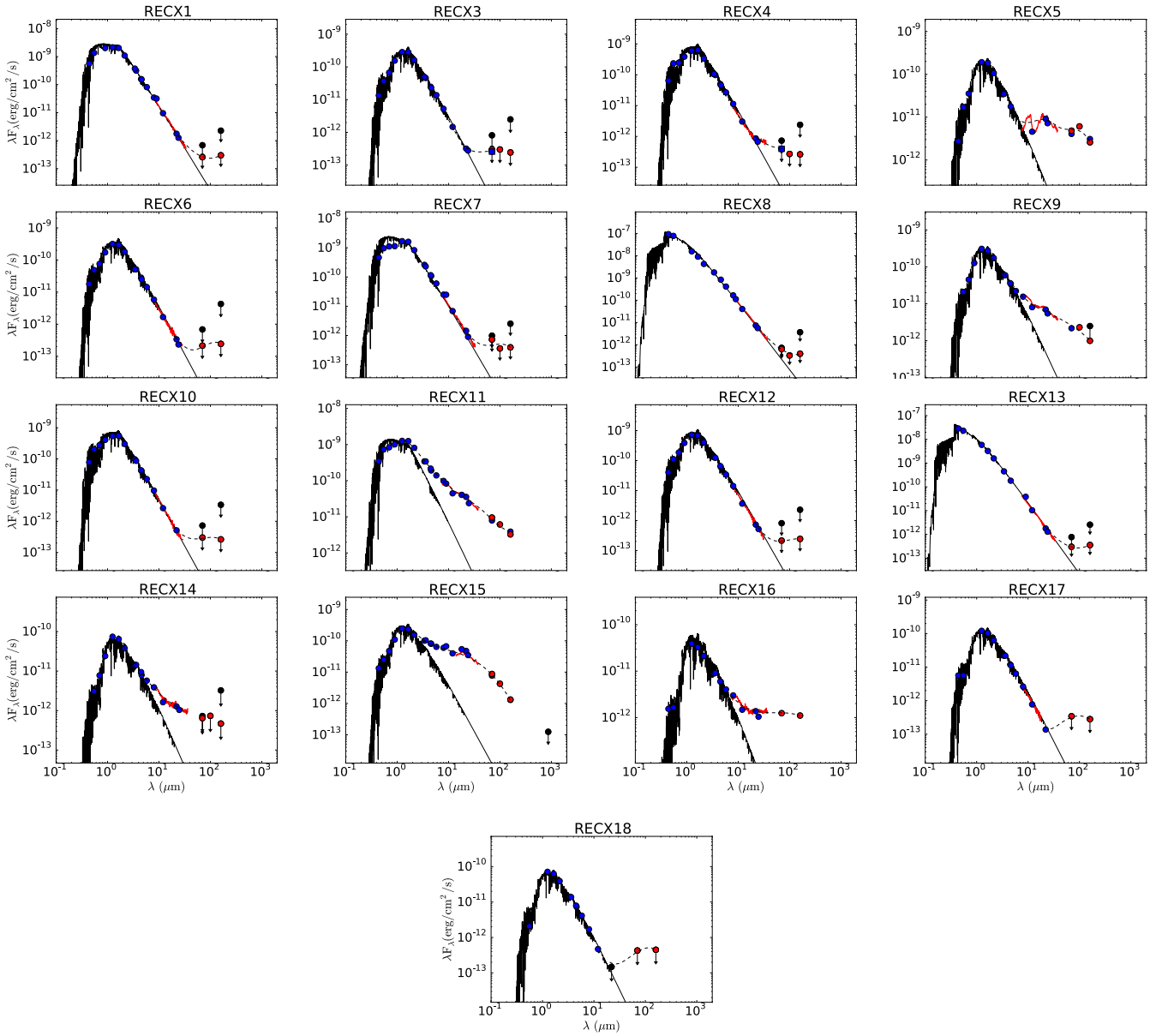

Fig. 8. SEDs of η Cha members observed with PACS photometry. PACS observations are shown as red dots. Blue dots depict photometry at different wavelengths from 2MASS, WISE, AKARI, and the literature (see Sect. 2). The blue squares in the RECX 3 and RECX 4 SEDs depict PACS photometry from Cieza et al. (2013). 3σ upper limits are shown as black arrows. The red curve depicts the IRS spectrum. The black solid curve is the photospheric model. The black dashed curve depicts the 3rd degree spline used to compute the infrared excess. The source names are shown at the top of each panel.

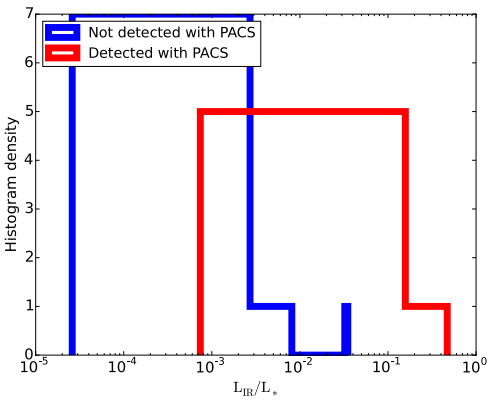

Fig. 9. Histogram showing the distribution of IR excesses for η Cha members observed with PACS.

Upper Scorpius. The SED of RECX 5 falls between the Taurus and Upper Scorpius median SED. The SED of RECX 9 is similar to the median SED in Upper Scorpius, but shows a comparably smaller flux at 160 μm. The RECX 11 and RECX 14 SEDs are similar to the median SED in Upper Scorpius up to 70 μm, but show smaller fluxes at longer wavelengths. RECX 16 show mid-IR fluxes that are between Taurus and Upper Scorpius, but far-IR fluxes similar to those in Taurus. Finally, RECX 15 shows near- and mid-IR fluxes typical of discs in Taurus, and far-IR fluxes similar to Upper Scorpius discs. Overall, η Cha SEDs show a variety of shapes for coeval discs, from Class II SEDs to debris discs. Sicilia-Aguilar et al. (2009) compared the median SED up to 24 μm of η Cha members with that of young stellar associations in the range 1 to 12 Myr. The authors computed different median SEDs for solar-type stars and M stars and concluded that the evolution of the SED depends on the spectral type.

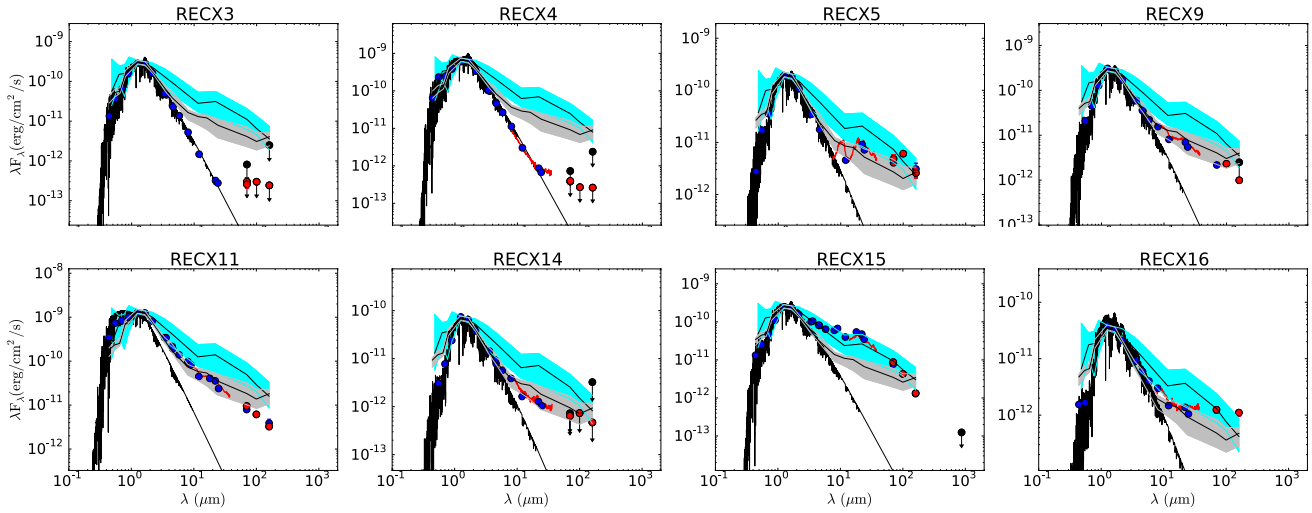

Fig. 10. SEDs of η Cha members detected with PACS photometry compared to the median SED in Taurus (cyan) and Upper Scorpius (grey) from Mathews et al. (2013). Blue dots depict archival photometry, while the red ones are PACS photometry from the present study. Black arrows are upper limits. The red curve depicts the IRS spectrum, while the black one represents the photospheric model.

5.2. Gas diagnostics in η Cha discs

5.2.1. Accretion and H_α profiles

The equivalent width (EW) of the H_α line has been traditionally used as an indicator of accretion. Lawson et al. (2004) performed the first study of accretion in η Cha. Based on the method by White & Basri (2003), they concluded that RECX 5, 9, 11, and 15 are still accreting at the age of η Cha. In a later study, Jayawardhana et al. (2006) concluded that RECX 9, 11, and 13 are accreting, but that RECX 5 is not. Therefore, observations of the same accretion indicator at different epochs can change the classification of a system, indicating that accretion is highly episodic. It must be noted, however, that η Cha members are active stars, and therefore flaring can also, and most likely does, contribute to EW variations in the Hα line.

We have gathered literature and archival data for low- and high-resolution spectroscopy (respectively) covering the H_α line for a total of 11 sources. We first discuss the estimations we can provide for the sample considering only the low-resolution spectroscopy, and second, the more detailed analysis conducted for targets with multiple epoch high-S/N, high-resolution spectroscopy.

We started our analysis by using the saturation criterion by Barrado y Navascués & Martín (2003), where the EW boundary between accretors and non-accretors is a function of spectral type (see Barrado y Navascués & Martín 2003, for a more detailed description of the method). In Fig. 11 we represent the H_α equivalent widths of η Cha members versus the spectral type, with H_α equivalent widths coming from Lawson et al. (2004) and Jayawardhana et al. (2006), as well as from UVES spectra analysed in this paper. We compile the equivalent widths from the literature and from the present work in Table 7. We have multiple epochs for all the targets but one, namely RECX 15. Therefore, we can study variability in accretion indicators. Among all the sources, RECX 4, RECX 5, RECX 11, and RECX 15 are actively accreting according to the saturation criterion in at least one epoch. RECX 4, RECX 5, and RECX 11 show highly variable H_α emission and no [OI] emission at 63 μm. For RECX 4, the average EW from all epochs is (4.4±3.7) Å, with a maximum value of 9.44 Å. In contrast, the average EW from non-accretion epochs is (2.8 ± 0.5) Å. In the case of RECX 5, the average EW from all epochs is (13 ± 10) Å with a maximum EW of 35.0 Å, while the average EW from non-accretion epochs is 9.2 ± 1.2 Å. RECX 11 is classified as an accreting system in one epoch, and falls near the boundary in the study by Lawson et al. (2004).

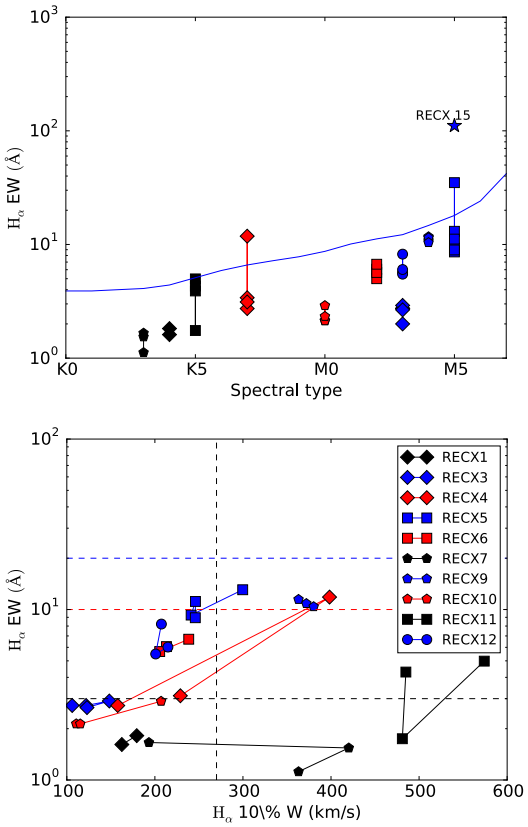

Fig. 11. *Top*: H_α equivalent width versus spectral type for η Cha members. The blue star gives the position of RECX 15 in the diagram. The solid curve represents the saturation criterion. *Bottom*: H_α equivalent width versus H_α 10% width. The vertical dashed line marks the position of the 10% velocity width limit for accretion.

Table 7. Compilation of equivalent widths, velocity widths at 10% of the H_α line, and mass accretion rates for η Cha members.

Source	*EW*	W-10%	log$\dot{M}_{acc}$	Epoch	Ref.
RECX	(Å)	(km s^{-1})	($M_\odot$/yr)	(dd/mm/yy)	
1	–1.2	103	–11.9		2
1	–1.82	179	–11.2	2011 Oct 15	1
1	–1.61	162	–11.3	2011 Oct 22	1
3	–2.0	116	–11.8		2
3	–2.2	85	–12.1		3
3	–2.74	106	–11.9	2011 Oct 15	1
3	–2.74	122	–11.7	2011 Oct 22	1
3	–2.91	148	–11.4	2011 Dec 13	1
3	–2.66	123	–11.7	2011 Dec 30	1
4	–3.4	147	–11.5		2
4	–2.3	105	–11.9		3
4	–2.73	158	–11.4	2011 Oct 22	1
4	–11.83	398	–9.02	2011 Dec 12	1
4	–3.12	229	–10.7	2012 Jan 06	1
5	–8.6	194	–11.0		2
5	–35.0	330	–9.7		3
5	–13.06	300	–10.0	2011 Dec 13	1
5	–9.28	241	–10.6	2011 Dec 30	1
5	–11.15	246	–10.5	2012 Jan 06	1
5	–8.95	246	–10.5	2012 Jan 07	1
6	–5.0	145	–11.5		2
6	–3.6	155	–11.4		3
6	–6.06	213	–10.8	2011 Dec 30	1
6	–5.67	205	–10.9	2012 Jan 07	1
6	–6.70	238	–10.6	2012 Jan 09	1
7	–1.0	291	–10.1		2
7	–0.4	120	–11.7		3
7	–1.12	363	–9.4	2011 Dec 15	1
7	–1.54	420	–8.8	2012 Jan 07	1
7	–1.66	193	–11.01	2012 Jan 09	1
9	–11.7	389	–9.1		2
9	–10.0	300	–10.0		3
9	–10.85	372	–9.3	2012 Jan 07	1
9	–11.46	363	–9.4	2012 Jan 09	1
9	–10.40	380	–9.2	2012 Jan 10	1
10	–1.2	102	–11.9		2
10	–1.0	110	–11.8		2
10	–2.14	112	–11.8	2011 Dec 15	1
10	–2.13	115	–11.7	2012 Jan 06	1
10	–2.90	207	–10.9	2012 Jan 07	1
11	–3.9	345	–9.5		2
11	–3.0	330	–9.7		3
11	–4.98	574	–7.3	2012 Jan 06	1
11	–1.75	481	–8.2	2012 Jan 07	1
11	–4.30	485	–8.2	2012 Jan 09	1
12	–5.7	154	–11.4		2
12	–4.2	160	–11.3		3
12	–8.22	207	–10.9	2011 Dec 15	1
12	–5.48	201	–10.9	2012 Jan 06	1
12	–6.02	215	–10.8	2012 Jan 07	1
15	–90	530	–7.7		3

References. (1): this work; (2): Jayawardhana et al. (2006); (3): Lawson et al. (2004).

Therefore, we have indications of episodic accretion in at least three η Cha members. Murphy et al. (2011) concluded that the variability of the H_α line in η Cha covers both short and long timescales, in agreement with what we see in the sample of UVES observations. RECX 15 is the only system detected in [OI] emission at 63 μm. RECX 9 was classified as an accreting system both by Lawson et al. (2004) and Jayawardhana et al. (2006), but it does not satisfy the saturation criterion.

For ten sources in the sample we have multi-epoch UVES archival observations of H_α at high resolution. The spectra of these sources around the H_α line are shown in Fig. 12. We used these observations to analyse accretion signatures in greater detail. The most prominent facts are the variety of profiles present and the high variability of the H_α line, regardless of the shape of the profile. We distinguish three groups of spectra according to the shape of the H_α emission. First, there is a group of simple double-peaked features, with peaks that are mostly symmetric, typical of chromospheric activity (see e.g. Frasca et al. 2008). This group includes RECX 1, RECX 3, RECX 6, RECX 10, and RECX 12. None of the sources in the first group have a detected IR excess, nor are they classified as actively accreting. Furthermore, their SEDs are photospheric at least until 30 μm, an indication that if any disc exists, it must be cold with a large inner gap devoid of dust.

The second group consist of features with a P Cygni profile indicative of the presence of an outflow, and RECX 11 is the only member. We note that RECX 11 shows a prominent excess starting at the near-IR.

The third group is made of single- or double-peaked profiles with high-velocity components and high variability, and includes RECX 4, RECX 5, and RECX 9. In the third group we find the most interesting profiles. First, RECX 4 shows high variability between different epochs, including one with high-velocity wings (EW = 9.4 compared to the average value of $\langle EW \rangle$ = 2.5 ± 0.1 from the other two UVES epochs), with velocities as high as 100 km s^{-1} in both the blue- and red-shifted part of the spectrum. This velocity is not high enough to conclude whether it is of stellar origin or due to winds and accretion. RECX 5 shows a blue-shifted component at ∼−150 km s^{-1} in one epoch, indicative of accretion. Finally, RECX 9 shows a single-peaked profile with a high-velocity blue-shifted wing at ∼−80 km s^{-1} and an isolated red-shifted feature around 100 km s^{-1}. The shape of the feature can be due to a very deep self-absorption on the red side of the spectra. All the stars in this group show mid-IR excess, while RECX 5 and RECX 9 also show far-IR excess. The variability of the line and the presence of high-velocity wings is likely due to the presence of infalling gas.

The spectra for RECX 7 are very hard to interpret, and so we treat them separately. The different epochs show prominent variability. RECX 7 has no detected excess, therefore the variability is purely chromospheric. Furthermore, RECX 7 is a double-lined spectroscopic binary (SB2, Lyo et al. 2003), which explains the broad shape of the line compared to its low equivalent width, as well as variability along the orbital phase.

To complement the qualitative comments in the previous paragraphs, we show in the bottom panel of Fig. 11 equivalent widths versus widths at 10% for the H_α line, together with the criterion by White & Basri (2003). Five η Cha members are accreting according to this criterion, namely RECX 4, RECX 5, RECX 7, RECX 9 and RECX 11. RECX 4 and RECX 5 show 10% widths in agreement with ongoing accretion in just on epoch, RECX 7 in two epochs, and RECX 9 and RECX 11 in all the available epochs. Interestingly, RECX 9 is not classified as an accretor when equivalent widths are used, but falls near the saturation criterion. The final list of sources with indications of accretion is then RECX 4, RECX 5, RECX 7, RECX 9, RECX 11, and RECX 15, and in at least three sources we have evidence of variable accretion, namely RECX 4, RECX 5, and RECX 11. Using the relation by Natta et al. (2004), we computed accretion rates for η Cha members. The resulting rates are shown in Table 7, and range from ∼10^{-12} $M_\odot$/yr for non-accretors to ∼10^{-8} $M_\odot$/yr for sources that are actively accreting.

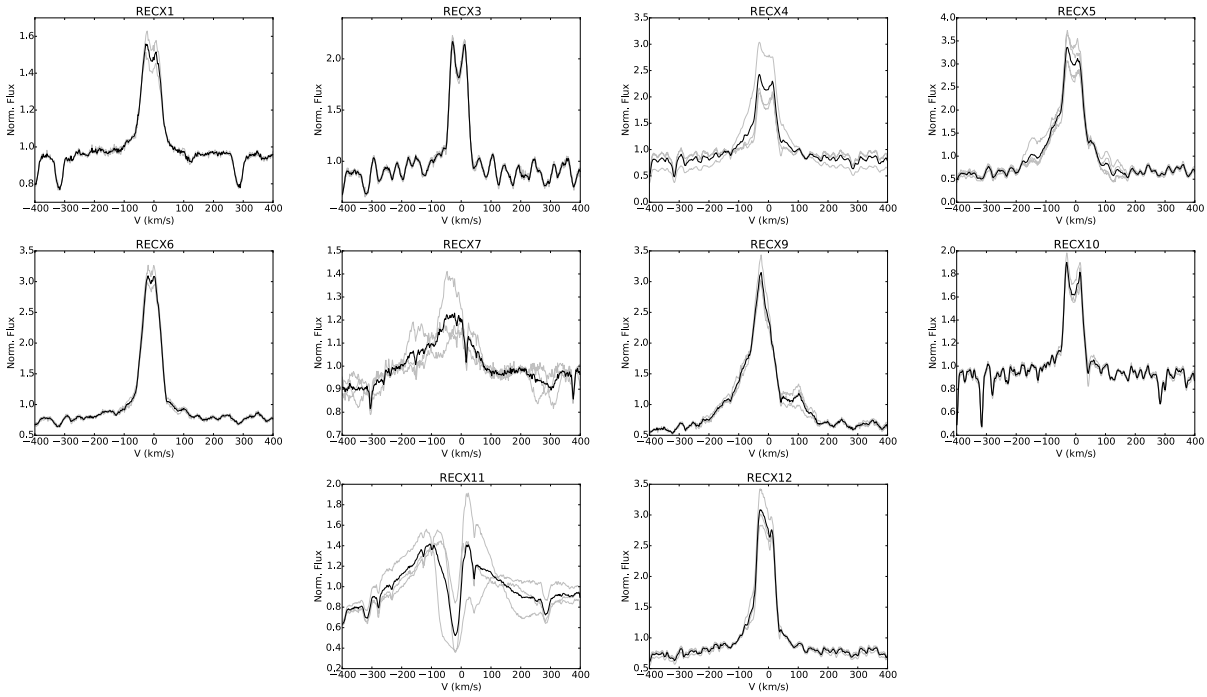

Fig. 12. UVES spectra of η Cha members at 6560 μm centred on the H_α line. Grey curves show individual epochs, while the black curve shows the average spectrum from all epochs.

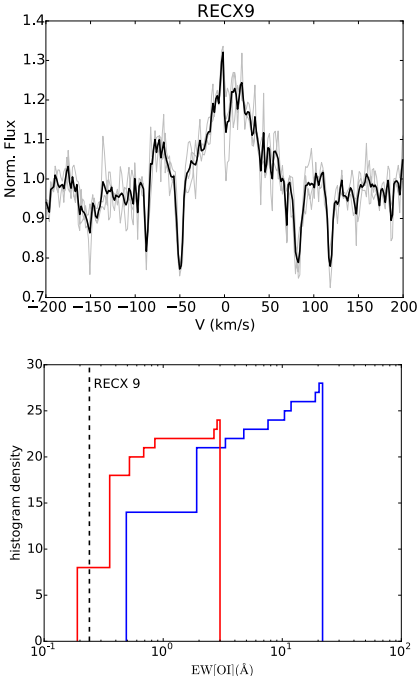

Fig. 13. *Top*: UVES spectra of RECX 9 members at 6300 Å centred on the [OI] line. Gray curves show individual epochs, while the black curve shows the average spectrum from all epochs. *Bottom*: cumulative histogram of [OI] EW at 6300 Å from Hartigan et al. (1995). Sources with an identified jet are shown in blue, while sources without a jet signature are shown in red. The vertical dashed line marks the position of RECX 9 [OI] EW at 6300 Å.

To further investigate gas properties and dynamics, we looked for [OI] emission at 6300 Å. However, only RECX 9 showed hints of emission (see Fig. 13). The emission is detected in all three epochs, with EW = 0.24,0.23, and 0.25 Å, with an average error of 0.05 Å. Hartigan et al. (1995) studied [OI] emission at 6300 Å in a sample of classical and weak T Tauri stars. In the bottom panel of Fig. 12 we show cumulative histograms of the [OI] EW at 6300 Å. The sample is divided into jet and non-jet sources following Howard et al. (2013). Equivalent widths for jet sources are in the range 0.5 to 22 Å, with a typical value around 4 Å, while non-jet sources show values in the range 0.2 to 3.0 Å. We therefore conclude that [OI] emission in RECX 9 is not associated with a jet.

5.2.2. Flattened discs and [OI] emission at 63 μm

Three parameters govern the [OI] flux at 63 μm in a protoplanetary disc: the total gas mass, the UV radiation field, and the flaring geometry of the disc (Woitke et al. 2010). Therefore, the lack of [OI] at 63 μm does not necessarily imply that they are gas empty. Rather, three alternative explanations are possible. First, these discs can be particularly flat, in agreement with the argument used by Gautier et al. (2008) to explain intermediate IR excesses in η Cha sources. Woitke et al. (2010) showed that for the same disc model, changing the flaring index from 1.0 to 1.2 results in an increase of almost two orders of magnitude in [OI] flux for the high-mass discs ($M_{\rm gas} > 10^{-4}\ M_\odot$). Keane et al. (2014) studied a sample of transitional discs observed with PACS and concluded that the lower [OI] luminosity in transitional discs can result either from a decrease in flaring or from a decrease in the gas-to-dust ratio, which strengthens the option that flat discs explain the lack of [OI] emission. An alternative explanation is a very weak UV field. A change in [OI] line flux similar to the one produced by the change in flaring index is produced when moving from low-UV models ($f_{\rm UV}$ = 0.001, where $f_{\rm UV}$ is the UV excess, defined as $f_{\rm UV} = L_{\rm UV}/L_*$) to high-UV models ($f_{\rm UV}$ = 0.1, see Fig. 2 in Woitke et al. 2010). The third option is that these discs are devoid of gas. A combination of the three scenarios can also explain the lack of [OI] emission.

An especially interesting case is that of η Cha members where we detected signs of accretion, yet no [OI] emission at 63 μm is observed (RECX 4, RECX 5, RECX 9,

and RECX 11). A similar case is TWA 03A – also known as Hen 3–600 – where no [OI] emission is detected, while H_α emission agrees with an actively accreting system (Riviere-Marichalar et al. 2013). The detection of active accretion favours the possibility of a high f_{UV} disc since the accretion luminosity correlates with the f_{UV} (Yang et al. 2012). However, the correlation is subject to large scatter and the previous conclusion is only valid from a statistical point of view, leaving open the possibility of active accretion with low f_{UV} in some systems. However, it is very unlikely that all the active accretors lacking [OI] emission show very low f_{UV} (~0.001). The most likely explanation for the lack of [OI] emission in these sources is then a flat disc. Alternative explanations have to face the problem of active accretion that is still ongoing, even if it is episodic.

Confirmation of the conclusions regarding transitional and/or flattened discs might come from high spatial resolution ALMA observations in the continuum, for insight into the dust geometry, and certain species like CO, which help to understand the gas distribution. The power of ALMA to solve the geometry of the disc by means of thermal emission and line emission maps has been demonstrated in recent years (see e.g. de Gregorio-Monsalvo et al. 2013; van der Marel et al. 2013).

5.2.3. Gas content in RECX 15

RECX 15 was already known to show [OI] emission at 63 μm (Woitke et al. 2011). However, no other far-IR line emission was detected in the source. According to our previous section, the system is actively accreting. Furthermore, the work of Lawson et al. (2004) indicates the presence of a blue-shifted component, likely attributable to a wind, and derives a mass accretion rate of 10^{-9} $M_\odot$/year. Ramsay Howat & Greaves (2007) detected H_2 emission at 2.1218 μm and derived a mass of hot gas of 5×10^{-9} $M_\odot$, almost one order of magnitude larger than the mass of hot gas that they derive for TW Hya. The authors concluded that the line was emitted by gas in Keplerian rotation at 2 AU from the central star. Observations of other six η Cha members were reported in the same study, with negative results, including RECX 5, 9, and 11.

Observations of the source at multiple wavelengths were used to model in detail the disc around RECX 15 by Woitke et al. (2011), including PACS line observations at 63 μm and range spectroscopic observations, PACS photometric observations, and observations of CO with APEX at 867 μm, amongst others. However, owing to the high number of non-detections, the authors could only derive a range of gas masses compatible with observations, $5 \times 10^{-5} < M_{gas}/M_\odot < 3 \times 10^{-3}$, and a gas-to-dust ratio of more than 2000.

The analysis of [OI] emission at 63 μm in Taurus sources by Howard et al. (2013) showed that it is correlated with the continuum emission at 63 μm, and that for the same continuum level, outflow sources show a higher [OI] flux. With a flux density of 0.204 Jy at 70 μm and line flux of 2.4×10^{-17} W/m^2, RECX 15 falls in the outflow region of the plot. The presence of blue-shifted components in the [OI] 6300 Å further suggests the presence of a jet or outflow (Woitke et al. 2011). Jet sources can show [OI] at 63 μm extended emission along the jet direction (Podio et al. 2012). However, we only detect [OI] emission in the central spaxel (see Fig. 7).

5.3. Multiplicity in η Cha

Multiplicity can have a huge impact on disc evolution (Kraus et al. 2012). In order to better place a context for the peculiar characteristics of the η Cha discs we have performed a detailed study of the multiplicity of our sample. Previous works looked for the presence of binaries in η Cha. As pointed out by Bouwman et al. (2006), the presence of a disc seems to be linked to single stars. In the following we summarise the results from previous studies:

- Köhler & Petr-Gotzens (2002) looked for visual binaries among η Cha members and detected companions for RECX 1 and RECX 9 at physical separations of ~17 and ~22 AU, respectively.
- Lyo et al. (2003) showed that RECX 7 is a spectroscopic binary with a projected physical separation of ~0.1 AU.
- Andersen (1975) concluded that RECX 8 is a spectroscopic binary with a projected separation of ~0.04 AU.
- Brandeker et al. (2006) shows that RECX 12 is a visual binary. From the asymmetric profile of the NACO image the authors derive a separation of ~0.″04.
- Brandeker et al. (2006) presented observations of all η Cha members except RECX 4, looking for visual companions using adaptive optics (AO) imaging with the nasmyth adaptive optics system (NACO) instrument. These observations were sensitive down to substellar and planetary-mass companions at angular separations of approximately 0.3″ and 0.5″. The authors concluded that there is a deficit of wide binaries at separations >20 AU in the cluster.

We now use the UVES radial velocity measurements from Sect. 3.3 to tackle the presence of close-in binaries among η Cha members. Multiple epochs were available for each of the ten objects (2–4 separate observations). This provides sensitivity to RV variations resulting from single-lined spectroscopic binaries (SB1s) as well as double- and potentially triple-lined spectroscopic binaries (SB2s and SB3s). The separation in time between these observations ranges from 1 day to 1 month. This uneven time sampling affects our sensitivity to systems of different configurations (inclination, mass, period). To account for the sensitivity in detecting binary systems as a result of our irregularly-spaced spectroscopic data we created a set of synthetic binary systems. We then characterise these systems using the dates of UVES observations and determine whether or not the RV variation would have been significant enough to be detected given the difference in time. Details of the methodology are described in Duquennoy & Mayor (1991) and more recently in Elliott et al. (2014). We used an average mass of the primary 0.5 $M_\odot$, the average sample mass using the evolutionary tracks of Baraffe et al. (1998), assuming an age of 7 Myr. The resulting analysis is shown in Fig. 14, where we represent the probability distribution for different combinations of period (P) and mass of the secondary (M_2). According to our calculations, we have a >60% probability of detecting companions with $M_2 \gtrsim 0.1$ $M_\odot$ in orbits with $P < 30$ d. Our results for η Cha members are the following.

- RECX 1: we find no evidence for new companions.
- RECX 3, 4, 5, 6, 10, and 11: no signs of multiplicity from imaging studies or from the present spectroscopic study.
- RECX 7: we confirm the presence of a spectroscopic binary. Deriving the orbital parameters is beyond the scope of this paper.
- RECX 9, 12: no signs of spectroscopic binaries

Four η Cha members with discs were covered by our multiplicity study: RECX4, RECX 5, RECX 9, and RECX 11. To our sensitivity limits ($M_2 \gtrsim 0.25$ $M_\odot$, $a \gtrsim 0.8$ AU), the claim by Bouwman et al. (2006) that circumstellar discs are linked

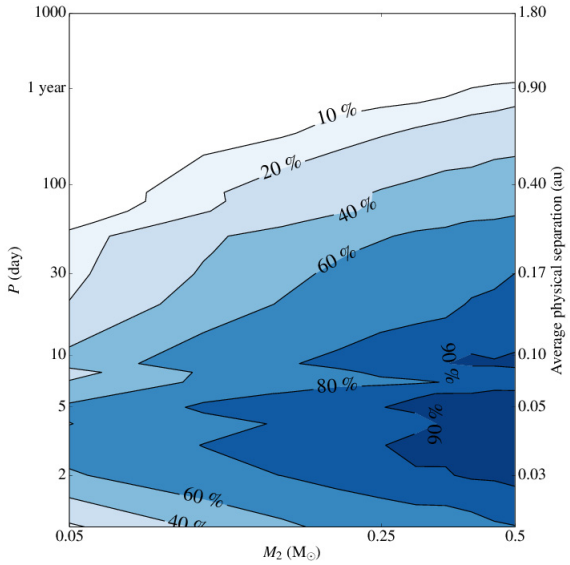

Fig. 14. Probability density maps for M_2.

to single stars remains true, with the exception of RECX 9. In total, we analysed UVES data for ten η Cha members and found only one spectroscopic binary, leading to a SB detection fraction of $0.10^{+0.17}_{-0.03}$ ($0.18^{+0.16}_{-0,06}$, if we include RECX 8 from Andersen 1975), compatible with the fractions found for the SACY (Search for Associations Containing Young stars, Torres et al. 2006) associations in Elliott et al. (2014), which are in the range 0.03–0.14. However, the lack of binaries wider that 20 AU is puzzling; none of the 17 members of the association studied by Brandeker et al. (2006) showed signs of wider binaries ($a > 20$ AU), leading to a detection fraction $0^{+0.1}$. In contrast, the detection fraction for SACY members in the same parameter space is $0.23^{+0.04}_{-0.03}$ (Elliott et al. 2015). The η Cha association is then a strange association in terms of the distribution of wide binaries. However, the difference is only 2σ, therefore it has to be considered with caution.

5.4. Disc evolution in η Cha

Discs in η Cha show a wide range of fractional disc luminosities, from $<10^{-3}$ to >0.1, which implies that both debris and primordial discs are found around coeval stars. Therefore, η Cha could represent an intermediate evolutionary stage for clusters where debris have started to form while primordial discs still survive, similar to TWA. This leaves open the possibility that the second generation dust from collisional grinding that constitutes debris discs forms while the primordial disc is still present.

One disc in the association, RECX 4, shows a fractional disc luminosity that is typical of debris discs while showing one epoch of active accretion (see Sect. 5.2.1), which makes it particularly interesting, since debris discs are thought to be gas empty or very poor. This could represent an intermediate stage between the exhaustion of the primordial disc and the formation of the debris disc, with second generation dust and primordial gas present at the same time. RECX 4 then joins the short list of old, second generation debris discs with accretion signatures detected so far (Looper et al. 2010a,b; Zuckerman et al. 2014; Reiners 2009).

The high number of infrared excess detections in η Cha (~50% Sicilia-Aguilar et al. 2009), as well as the shape of the SED for detected sources, challenges our knowledge of disc evolution as most of the circumstellar material is supposed to dissipate in timescales shorter than the age of the association. According to Sicilia-Aguilar et al. (2006), 50% of low-mass stars lose their near- and mid-IR excesses by 3 Myr. Most sources in η Cha do not show near-IR excess, RECX 11 and 15 being the exceptions. However, 50% of the cluster members show mid-IR excess, indicative of the presence of a warm disc. At 70 μm the detection fraction is $0.33^{+0.13}_{-0.10}$, compatible with the mid-IR fractions when uncertainties are included. Fang et al. (2013) shows that disc evolution and dispersal proceeds slowly in loose stellar associations compared to denser ones. At an age of 7 Myr, η Cha circumstellar show a variety of properties, from primordial discs with an IR excess more prominent than the median SED in Taurus to debris discs. The presence of primordial discs agrees well with η Cha also being a loose stellar association where the evolution proceeds slowly. According to the study by Ribas et al. (2014), however, the detection fraction in η Cha seems to fit within the general behaviour (see Fig. 2 in Ribas et al. 2014). This study was based in mid-IR detection fractions, which tend to be lower than the far-IR detection fractions due to the detection of a population of debris discs that are unseen in the mid-IR. However, this does not affect the detection fraction of primordial discs ($0.35^{+0.12}_{-0.09}$), since debris discs are second generation. Furthermore, the disc fraction in η Cha could change in the future if undiscovered members are detected (see SecT. 1). A complete census of η Cha members is needed to tackle the problem of the different timescale in loose environments.

6. Summary

We have observed 17 members of the η Cha cluster with PACS in photometric mode at 70, 100, and 160 μm. A subsample of 13 members was also observed in line spectroscopic mode, aiming to detect [OI] and o-H_2O emission at 63 μm. Three sources in this subsample were also observed with PACS in range spectroscopic mode. The main results and conclusions of the present study are as follows:

1) We detected four out of sixteen discs observed at 70 μm, four out of eight at 100 μm, and five out of seventeen at 160 μm, leading to a far-IR excess detection fraction of $0.29^{+0.13}_{-0.08}$.
2) We detected [OI] emission towards RECX 15. The emission is not extended, but the position of the source in a $F_{[OI],63\ \mu m}$ versus $F_{70\ \mu m}$ diagram is consistent with outflow sources.
4) η Cha members show a variety of SEDs, including Class II discs, transitional discs, and debris discs. The survival of transitional and primordial discs could be linked to the loose nature of the η Cha, as proposed by previous authors.
5) We studied H_α profiles and computed equivalent widths, finding accretion signatures in RECX 4, 5, 9, 11, and 15.
6) We have detected signatures of accretion in one debris disc in the association, namely RECX 4. This is one of the few cases where active accretion is found around a debris disc.
7) The intermediate IR excess shown by RECX 5, RECX 9, and RECX 16 can be explained as the result of a flattened geometry, which can also explain the lack of [OI] detections for these sources. The cases of RECX 5 and RECX 9 are especially challenging as they show signs of episodic accretion, indicating the presence of gas. A flat disc can easily explain the detection of episodic accretion together with the lack of [OI] emission. However, it is also possible that the gas clearing timescale is shorter than the dust timescale. Furthermore, low UV irradiation can also be responsible for the lack of [OI] detections in some sources.
8) We looked for close-in companions of η Cha members in UVES data and found no new spectroscopic binaries among

ten η Cha members studied. We confirmed that RECX 7 is a spectroscopic binary. The fraction of spectroscopic binaries is then $0.18^{+0.16}_{-0.06}$, compatible with other nearby associations. No disc is found around spectroscopic binaries in η Cha.

Acknowledgements. P.R.M. acknowledges funding from the ESA Research Fellowship Programme. A.B. acknowledges financial support from the Proyecto Fondecyt de Iniciación 11140572 and support from the Millenium Science Initiative, Chilean Ministry of Economy, Nucleus RC130007. I.K. acknowledges funding from the European Union Seventh Framework Programme FP7-2011 under grant agreement No. 284405. This publication makes use of VOSA, developed under the Spanish Virtual Observatory project supported from the Spanish MICINN through grant AyA2011-24052. A.R. acknowledges funding from the ESAC Science Operations Division research funds with code SC 1300016149 and support from the ESAC Space Science Faculty.

References

Aikawa, Y., Miyama, S. M., Nakano, T., & Umebayashi, T. 1996, ApJ, 467, 684
Andersen, J. 1975, A&A, 44, 445
Balog, Z., Müller, T., Nielbock, M., et al. 2014, Exp. Astron., 37, 129
Baraffe, I., Chabrier, G., Allard, F., & Hauschildt, P. H. 1998, A&A, 337, 403
Barrado y Navascués, D., & Martín, E. L. 2003, AJ, 126, 2997
Bayo, A., Rodrigo, C., Barrado y Navascués, D., et al. 2008, A&A, 492, 277
Bayo, A., Rodrigo, C., Barrado, D., et al. 2014, in ASI Conf. Ser., 11, 93
Bessel, M. S. 1990, A&AS, 83, 357
Bouwman, J., Lawson, W. A., Dominik, C., et al. 2006, ApJ, 653, L57
Brandeker, A., Jayawardhana, R., Khavari, P., Haisch, Jr., K. E., & Mardones, D. 2006, ApJ, 652, 1572
Burgasser, A. J., Kirkpatrick, J. D., Reid, I. N., et al. 2003, ApJ, 586, 512
Cieza, L. A., Olofsson, J., Harvey, P. M., et al. 2013, ApJ, 762, 100
de Gregorio-Monsalvo, I., Ménard, F., Dent, W., et al. 2013, A&A, 557, A133
Dent, W. R. F., Thi, W. F., Kamp, I., et al. 2013, PASP, 125, 477
Duquennoy, A., & Mayor, M. 1991, A&A, 248, 485
Elliott, P., Bayo, A., Melo, C. H. F., et al. 2014, A&A, 568, A26
Elliott, P., Huélamo, N., Bouy, H., et al. 2015, A&A, 580, A88
Fang, M., van Boekel, R., Bouwman, J., et al. 2013, A&A, 549, A15
Frasca, A., Kovári, Z., Strassmeier, K. G., & Biazzo, K. 2008, A&A, 481, 229
Freedman, D., & Diaconis, P. 1981, Z. Wahrscheinlichkeitstheorie und Verwandte Gebiete, 57, 453
Gautier, III, T. N., Rebull, L. M., Stapelfeldt, K. R., & Mainzer, A. 2008, ApJ, 683, 813
Gorti, U., & Hollenbach, D. 2008, ApJ, 683, 287
Hartigan, P., Edwards, S., & Ghandour, L. 1995, ApJ, 452, 736
Howard, C. D., Sandell, G., Vacca, W. D., et al. 2013, ApJ, 776, 21
Ishihara, D., Onaka, T., Kataza, H., et al. 2010, A&A, 514, A1
Jayawardhana, R., Coffey, J., Scholz, A., Brandeker, A., & van Kerkwijk, M. H. 2006, ApJ, 648, 1206
Keane, J. T., Pascucci, I., Espaillat, C., et al. 2014, ApJ, 787, 153
Köhler, R., & Petr-Gotzens, M. G. 2002, AJ, 124, 2899
Kraus, A. L., Ireland, M. J., Hillenbrand, L. A., & Martinache, F. 2012, ApJ, 745, 19
Lada, C. J. 1987, in Star Forming Regions, eds. M. Peimbert, & J. Jugaku, IAU Symp., 115, 1
Lawson, W. A., Crause, L. A., Mamajek, E. E., & Feigelson, E. D. 2001, MNRAS, 321, 57
Lawson, W. A., Lyo, A.-R., & Muzerolle, J. 2004, MNRAS, 351, L39
Lebouteiller, V., Barry, D. J., Spoon, H. W. W., et al. 2011, ApJS, 196, 8
Looper, D. L., Bochanski, J. J., Burgasser, A. J., et al. 2010a, AJ, 140, 1486
Looper, D. L., Mohanty, S., Bochanski, J. J., et al. 2010b, ApJ, 714, 45
Luhman, K. L., & Steeghs, D. 2004a, ApJ, 609, 917
Lyo, A.-R., Lawson, W. A., Mamajek, E. E., et al. 2003, MNRAS, 338, 616
Lyo, A.-R., Lawson, W. A., Feigelson, E. D., & Crause, L. A. 2004, MNRAS, 347, 246
Lyo, A.-R., Song, I., Lawson, W. A., Bessell, M. S., & Zuckerman, B. 2006, MNRAS, 368, 1451
Mamajek, E. E., Lawson, W. A., & Feigelson, E. D. 1999, ApJ, 516, L77
Mathews, G. S., Pinte, C., Duchêne, G., Williams, J. P., & Ménard, F. 2013, A&A, 558, A66
McJunkin, M., France, K., Schneider, P. C., et al. 2014, ApJ, 780, 150
Megeath, S. T., Hartmann, L., Luhman, K. L., & Fazio, G. G. 2005, ApJ, 634, L113
Murphy, S. J., Lawson, W. A., & Bessell, M. S. 2010, MNRAS, 406, L50
Murphy, S. J., Lawson, W. A., Bessell, M. S., & Bayliss, D. D. R. 2011, MNRAS, 411, L51
Natta, A., Testi, L., Muzerolle, J., et al. 2004, A&A, 424, 603
Pinte, C., & Laibe, G. 2014, A&A, 565, A129
Podio, L., Kamp, I., Flower, D., et al. 2012, A&A, 545, A44
Queloz, D., Dubath, P., & Pasquini, L. 1995, A&A, 300, 31
Ramsay Howat, S. K., & Greaves, J. S. 2007, MNRAS, 379, 1658
Reiners, A. 2009, ApJ, 702, L119
Ribas, Á., Merín, B., Bouy, H., & Maud, L. T. 2014, A&A, 561, A54
Riviere-Marichalar, P., Pinte, C., Barrado, D., et al. 2013, A&A, 555, A67
Riviere-Marichalar, P., Barrado, D., Montesinos, B., et al. 2014, A&A, 565, A68
Riviere-Marichalar, P., Bayo, A., Kamp, I., et al. 2015, A&A, 575, A19
Sicilia-Aguilar, A., Hartmann, L., Calvet, N., et al. 2006, ApJ, 638, 897
Sicilia-Aguilar, A., Bouwman, J., Juhász, A., et al. 2009, ApJ, 701, 1188
Skrutskie, M. F., Dutkevitch, D., Strom, S. E., et al. 1990, AJ, 99, 1187
Skrutskie, M. F., Cutri, R. M., Stiening, R., et al. 2006, AJ, 131, 1163
Soderblom, D. R., Hillenbrand, L. A., Jeffries, R. D., Mamajek, E. E., & Naylor, T. 2014, Protostars and Planets VI, 219
Song, I., Zuckerman, B., & Bessell, M. S. 2004, ApJ, 600, 1016
Strom, K. M., Strom, S. E., Edwards, S., Cabrit, S., & Skrutskie, M. F. 1989, AJ, 97, 1451
Thi, W.-F., Mathews, G., Ménard, F., et al. 2010, A&A, 518, L125
Torres, C. A. O., Quast, G. R., da Silva, L., et al. 2006, A&A, 460, 695
van der Marel, N., van Dishoeck, E. F., Bruderer, S., et al. 2013, Science, 340, 1199
White, R. J., & Basri, G. 2003, ApJ, 582, 1109
Williams, J. P., & Best, W. M. J. 2014, ApJ, 788, 59
Williams, J. P., & Cieza, L. A. 2011, ARA&A, 49, 67
Woitke, P., Pinte, C., Tilling, I., et al. 2010, MNRAS, 405, L26
Woitke, P., Riaz, B., Duchêne, G., et al. 2011, A&A, 534, A44
Wright, E. L., Eisenhardt, P. R. M., Mainzer, A. K., et al. 2010, AJ, 140, 1868
Yang, H., Herczeg, G. J., Linsky, J. L., et al. 2012, ApJ, 744, 121
Zuckerman, B., & Song, I. 2004, ARA&A, 42, 685
Zuckerman, B., Vican, L., & Rodriguez, D. R. 2014, ApJ, 788, 102